

# London equation studies of thin-film superconductors with a triangular antidot lattice

Sa-Lin Cheng<sup>1</sup>, D. J. Priour Jr<sup>1,2</sup>, H. A. Fertig<sup>1</sup>

<sup>1</sup>*Department of Physics and Astronomy, University of Kentucky, Lexington, KY40506-0055*

<sup>2</sup>*Center for Computational Sciences, University of Kentucky, Lexington, KY40506-0045*

(November 1, 2018)

We report on a study of vortex pinning in nanoscale antidot defect arrays in the context of the London Theory. Using a wire network model, we discretize the array with a fine mesh, thereby providing a detailed treatment of pinning phenomena. The use of a fine grid has enabled us to examine both circular and elongated defects, patterned in the form of a rhombus. The latter display pinning characteristics superior to circular defects constructed with the similar area. We calculate pinning potentials for defects containing zero and single quanta, and we obtain a pinning phase diagram for the second matching field,  $H = 2\Phi_0$ .

PACS numbers: 74.20.-z, 74.60.Ge, 74.76.-w, 68.55.Ln, 61.46.+w

## I. INTRODUCTION

It has long been known that defects in superconductors can act as pinning centers for vortices. The trapping of vortices reduces dissipation and permits higher critical currents, which is important in engineering applications involving superconductors. In nature, one expects defects to be randomly distributed within a sample. To examine vortex pinning in a more controlled setting, a body of experimental work has examined pinning phenomena in artificial defect arrays. Advances in sub-micron lithography<sup>1-4</sup> permit the construction of artificial nanoscale defect arrays. Lorentz microscopy permits direct imaging<sup>5</sup> of the magnetic fields associated with the vortices and supercurrents. Scanning Hall probes<sup>9,10</sup> provide less detail, albeit over a greater spatial range. The defects can be fashioned as regions of excised superconductor, “antidots”, or they may consist of ferromagnetic inclusions. This study concentrates on the antidot case.

The recent experimental work<sup>5-8</sup> on nanoscale defect arrays in thin films has motivated a number of theoretical studies<sup>11-14</sup> of pinning phenomena in them. In this vein, we offer a detailed numerical treatment of thin-film periodic antidot arrays in the context of the London theory<sup>17</sup>. Our study differs from most previous theoretical work in that it explicitly treats the thin-film geometry, rather than a bulk system with two dimensional ordering. Although we report on results obtained for the triangular antidot lattice, our method can readily be adapted to other geometries such as the square lattice. It is also within the scope of our method to consider more general inclusions, such as nanoscale defects with a permanent magnetic moment.

Since the London Theory does not admit a solution in closed form for our system, a numerical approach is needed. In our case, the numerical treatment involves solving the London equations in discrete form. In doing so, we model the supercurrents in our system as a wire network. To satisfy the zero-current constraint within the inclusions, we expand the current in terms of elements of a special basis, to be described in greater detail in the next section. To determine the optimum current

configuration, we minimize the discretized version of the London free energy with respect to the basis expansion coefficients.

## Synopsis of the results

As shall be discussed, our method permits us to compute the free energy for systems containing a fixed number of vortices at predetermined positions. By computing the London energy for different vortex configurations, we calculate the pinning potential for the vortices. Pinning potentials computed for different antidot radii indicate that pinning centers with radii larger than  $\xi(T)$  are more efficient at pinning than those whose size is in the vicinity of the coherence length. This result is in agreement with one of the experiments<sup>7</sup> as well as theoretical work<sup>15</sup> on three dimensional superconductors containing columnar defects. The pinning potentials also allow one to identify interstitial pinning. With the aid of pinning potentials, we have produced a phase plot displaying the optimum number of pinned vortices as a function of defect radius. A salient feature is the weak dependence of the number of pinned quanta on the effective magnetic penetration depth,  $\lambda_{eff}$ . Finally, we have examined the pinning potentials of defects with an elongated shape. To consider defects with sharp corners, we have studied antidots in the shape of a rhombus. Two notable features of the pinning potentials of rhombic defects are a lower pinning energy and a higher escape barrier than that of circular defects of comparable area, qualities indicating that the rhombus is superior to the circle as a pinning center.

The article is organized as follows: In Section II, we present the wire network model for the supercurrents in the nanoscale defect array. Section III outlines our methods for calculating the London free energies and current configurations, and Section IV reports our primary results. We conclude in Section V with a summary.

## II. THE MODEL

To proceed, we consider antidots of radius  $R$  forming a regular triangular lattice in a thin-film superconductor as shown in Fig. 1. The distance between dots is  $T_0$ .

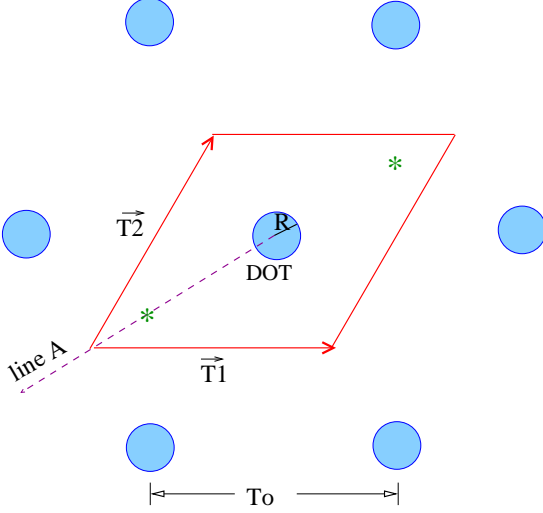


FIG. 1. The triangular lattice with lattice constant  $T_0$ .  $\vec{T}_1$  and  $\vec{T}_2$  are the primitive lattice vectors.  $\vec{T}_1 = T_0\hat{x}$ ,  $\vec{T}_2 = \frac{1}{2}T_0\hat{x} + \frac{\sqrt{3}}{2}T_0\hat{y}$ . The asterisks indicate the centers of the triangular plaquettes defined by the dots.

Since the London theory cannot be solved in closed form for our system, we discretize the space of the unit cell including the region of the dot by dividing each edge of the unit cell into  $N$  intervals. The locations of the  $N \times N$  *grid* points are given by

$$\vec{X}_{n_1, n_2} = \frac{n_1}{N}\vec{T}_1 + \frac{n_2}{N}\vec{T}_2, \quad 0 \leq n_1, n_2 < N. \quad (1)$$

The corresponding reciprocal lattice vectors are

$$\vec{G}_{m_1, m_2} = m_1\vec{W}_1 + m_2\vec{W}_2, \quad 0 \leq m_1, m_2 < N, \quad (2)$$

where  $\vec{W}_1$  and  $\vec{W}_2$  are the primitive vectors of the reciprocal lattice.

Having discretized the space and defined the grid points, we now construct the current network of the unit cell. First, we define

- *Nodes*: located at the center of each triangular plaquette formed by the three closest grid points. These nodes form a honeycomb lattice.
- *Links*: are the edges of the honeycomb lattice. The link midpoints are located at the intersection of the links and the plaquette edges.

We model our system as a wire network. Hence, the currents  $\vec{J}_s(\vec{X})$  only flow on the links. [See Fig. 2 and Fig. 3.]

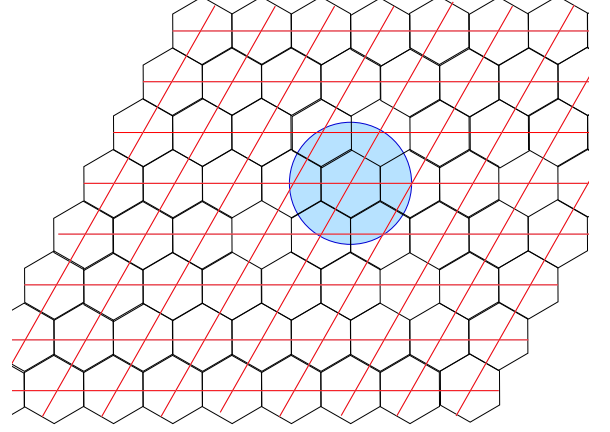


FIG. 2. The links form a honeycomb lattice, and the current only flows on links.

Fig. 3 illustrates a detailed section of our wire network. Three current links are associated with each grid point  $\vec{X}$ , which may be written as

$$\vec{J}_s(\vec{X}) = \begin{bmatrix} \vec{J}_{s1}(\vec{X}) \\ \vec{J}_{s2}(\vec{X}) \\ \vec{J}_{s3}(\vec{X}) \end{bmatrix}, \quad (3)$$

where  $\vec{J}_{s1}(\vec{X})$  is centered at  $\vec{X} + \frac{1}{2}\vec{a}_1$ ,  $\vec{J}_{s2}(\vec{X})$  at  $\vec{X} + \frac{1}{2}\vec{a}_2$  and  $\vec{J}_{s3}(\vec{X})$  at  $\vec{X} + \frac{1}{2}(\vec{a}_1 + \vec{a}_2)$ , with  $\vec{a}_1 = \frac{1}{N}\vec{T}_1$  and  $\vec{a}_2 = \frac{1}{N}\vec{T}_2$ .

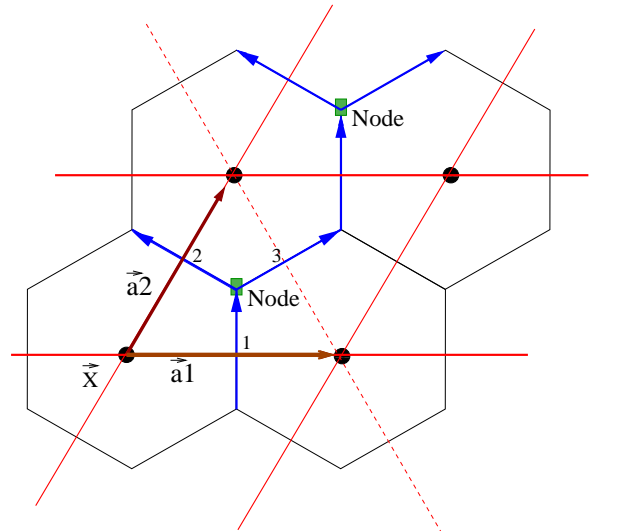


FIG. 3. Currents are depicted for the point  $\vec{X}$ . Current conservation requires that  $\vec{J}_{s1} = \vec{J}_{s2} + \vec{J}_{s3}$ .

We now enforce current conservation at the nodes. This gives two equations per grid cell (i.e., the cell formed by  $\vec{a}_1$  and  $\vec{a}_2$ ).

$$\vec{J}_{s1}(\vec{X}) = \vec{J}_{s2}(\vec{X}) + \vec{J}_{s3}(\vec{X}) \quad (4)$$

and

$$\vec{J}_{s3}(\vec{X}) + \vec{J}_{s2}(\vec{X} + \vec{a}_1) = \vec{J}_{s1}(\vec{X} + \vec{a}_2). \quad (5)$$

After Fourier transforming Eq.(4) and (5), we find that the current can be written in Fourier space as

$$\vec{J}_s(\vec{G}) = \begin{bmatrix} 1 - e^{-i\vec{G}\cdot\vec{a}_1} \\ 1 - e^{-i\vec{G}\cdot\vec{a}_2} \\ e^{-i\vec{G}\cdot\vec{a}_2} - e^{-i\vec{G}\cdot\vec{a}_1} \end{bmatrix} \Phi(\vec{G}), \quad \vec{G} \neq 0. \quad (6)$$

Since there is no net current flowing in the superconductor, we have to include the  $\vec{G} = 0$  component. Therefore, the current at the grid point  $\vec{X}$  can be written as

$$\vec{J}_s(\vec{X}) = j_{01} \begin{bmatrix} 1 \\ 0 \\ 1 \end{bmatrix} + j_{02} \begin{bmatrix} 1/\sqrt{3} \\ 2/\sqrt{3} \\ -1/\sqrt{3} \end{bmatrix} + \sum_{\vec{G} \neq 0} \begin{bmatrix} 1 - e^{-i\vec{G}\cdot\vec{a}_1} \\ 1 - e^{-i\vec{G}\cdot\vec{a}_2} \\ e^{-i\vec{G}\cdot\vec{a}_2} - e^{-i\vec{G}\cdot\vec{a}_1} \end{bmatrix} \Phi(\vec{G}) e^{-i\vec{G}\cdot\vec{X}}. \quad (7)$$

We can think of

$$\begin{bmatrix} j_{01} \\ j_{02} \\ \Phi(\vec{G}_1) \\ \Phi(\vec{G}_2) \\ \vdots \\ \Phi(\vec{G}_{N-1}) \end{bmatrix}$$

as a vector, whose entries are determined by the current distribution in the unit cell. Since we are considering systems with antidots, one must have no current flowing in the defects. As will be discussed in greater detail in the following section, we impose this no-current constraint by expressing the current as a linear combination of elements of a specially constructed basis. The elements of this basis are themselves current distributions satisfying the no-current constraint and are conveniently expressed via the vector formalism mentioned above. The basis elements span the set of all current configurations for which current is excluded from the defects.

### III. THE METHOD

Generally speaking, one calculates current distributions by minimizing the London free energy subject to

certain constraints, including the absence of current in the defects and a fixed number of vortices per unit cell. This shall be our program as well. Therefore, we first write the free energy per unit cell of our superconducting system in the London approximation,

$$F = \frac{2\pi\lambda_{eff}}{c^2} \sum_{\vec{X}} |\vec{J}_s(\vec{X})|^2 + \frac{1}{2c} \sum_{\vec{X}} \vec{J}_s(\vec{X}) \cdot \vec{A}_{tot}(\vec{X}). \quad (8)$$

In a thin-film superconductor, if the thickness is much smaller than the London penetration depth (i.e.,  $d \ll \lambda$ ), the volume current density  $\vec{J}$  is nearly constant in the thickness, so it is appropriate to write  $\vec{J}_s = \vec{J}d$  and define  $\lambda_{eff} = \lambda^2/d$ . The first term in Eq.(8) is the kinetic energy of the supercurrent, and the second term is the magnetic field energy, which is the sum of the contributions of the supercurrent itself ( $\vec{J}_s(\vec{X}) \cdot \vec{A}_s(\vec{X})$ ) and the interaction between the supercurrent and the external field ( $\vec{J}_s(\vec{X}) \cdot \vec{A}_{ext}(\vec{X})$ ). However, symmetry arguments indicate that the latter term vanishes in the case of thin-film superconductors. Since the currents are localized at the link midpoints, we only need to evaluate the dot product in Eq.(8) at the three midpoints in each grid cell. Hence, the free energy can be written as

$$\begin{aligned} F &= \frac{2\pi\lambda_{eff}}{c^2} \sum_{\vec{X}} \sum_{j=1}^3 |\vec{J}_s^j(\vec{X})|^2 \\ &+ \frac{1}{2c} \sum_{\vec{X}} \sum_{j=1}^3 \vec{J}_s^j(\vec{X}) \cdot \vec{A}_s^j(\vec{X}) \\ &= \frac{2\pi\lambda_{eff}}{c^2} \sum_{\vec{G}} \sum_{j=1}^3 |\vec{J}_s^j(\vec{G})|^2 \\ &+ \frac{1}{2c} \sum_{\vec{G}} \sum_{j=1}^3 \vec{J}_s^j(\vec{G}) \cdot [\vec{A}_s^j(\vec{G})]^*. \end{aligned} \quad (9)$$

In the rest of this section, we will briefly outline our method for solving the London theory for our system.

#### A. Constructing the current basis

To generate a basis satisfying the no-current condition in the defect region, we consider a functional which penalizes currents in this region. A simple choice is

$$W[\vec{J}_s] = V_0 \sum_{\vec{X}_0} |\vec{J}_s(\vec{X}_0)|^2, \quad (10)$$

where the  $\vec{X}_0$ 's are the points inside the dot, and  $V_0$  is a constant. We want to minimize  $W[\vec{J}_s]$  subject to the constraint that the current in the unit cell is normalized. We can implement this constraint by adding a Lagrangian multiplier to  $W[\vec{J}_s]$ . The result is a new functional  $\mathcal{L}$ ,

$$\mathcal{L} = V_0 \sum_{\vec{X}_0} |\vec{J}_s(\vec{X}_0)|^2 - \Lambda \left\{ \sum_{\vec{X}} |\vec{J}_s(\vec{X})|^2 - 1 \right\}. \quad (11)$$

If we write the supercurrent as a Fourier sum, plug Eq.(6) into Eq.(11), and carry out the sum in real space, we obtain  $\mathcal{L}$  is a function of  $j_{01}, j_{02}$  and  $\Phi(\vec{G})$ . Reality of  $\vec{J}_s(\vec{X})$  implies that  $\Phi(-\vec{G}) = \Phi^*(\vec{G})$ . This symmetry reduces sums over  $\vec{G}$  to sums over  $\vec{G} > 0$ . Next, we write  $\Phi(\vec{G}) = \Phi_{re}(\vec{G}) + i\Phi_{im}(\vec{G})$  and minimize  $\mathcal{L}$  with respect to  $j_{01}, j_{02}, \Phi_{re}(\vec{G})$  and  $\Phi_{im}(\vec{G})$ . This gives us four linear equations, which can be written as a matrix equation as Eq.(12) to solve for  $j_{01}, j_{02}, \Phi_{re}(\vec{G})$  and  $\Phi_{im}(\vec{G})$ .

$$M[\vec{G}, \vec{G}'] \begin{bmatrix} j_{01} \\ j_{02} \\ \Phi_{re}(\vec{G}'_1) \\ \vdots \\ \Phi_{re}(\vec{G}'_{(N^2-1)/2}) \\ \Phi_{im}(\vec{G}'_1) \\ \vdots \\ \Phi_{im}(\vec{G}'_{(N^2-1)/2}) \end{bmatrix} = \epsilon \begin{bmatrix} j_{01} \\ j_{02} \\ \Phi_{re}(\vec{G}_1) \\ \vdots \\ \Phi_{re}(\vec{G}_{(N^2-1)/2}) \\ \Phi_{im}(\vec{G}_1) \\ \vdots \\ \Phi_{im}(\vec{G}_{(N^2-1)/2}) \end{bmatrix}, \quad (12)$$

where  $M[\vec{G}, \vec{G}']$  is an  $(N^2 + 1) \times (N^2 + 1)$  matrix, and  $\epsilon \propto \Lambda/V_0$ .

After solving the eigenequation, we obtain  $(N^2 + 1)$  eigenvalues. The eigenvalues exhibit a clear hierarchy. Fig. 4 is an example for  $N = 11$  with  $R = 55nm$ .  $q$  values are very high relative to the other  $N^2 + 1 - q$  eigenvalues. The large eigenvalues correspond to eigenstates for which currents within the defect are nonzero. Excluding these eigenstates allows us to construct a basis satisfying the no-current condition. This can be done by inserting the entries of the eigenvector into Eq.(7)., yielding  $3 \times (N^2 + 1 - q)$  real space versions of the basis elements  $\vec{J}_n^j(\vec{X})$  for  $n = 1, 2, \dots, (N^2 + 1 - q)$ , and  $j = 1, 2, 3$ . Any component of the current distribution can be expressed as a linear combination of the basis elements, i.e.,  $\vec{J}^j(\vec{X}) = \sum_n v_n \vec{J}_n^j(\vec{X})$ .

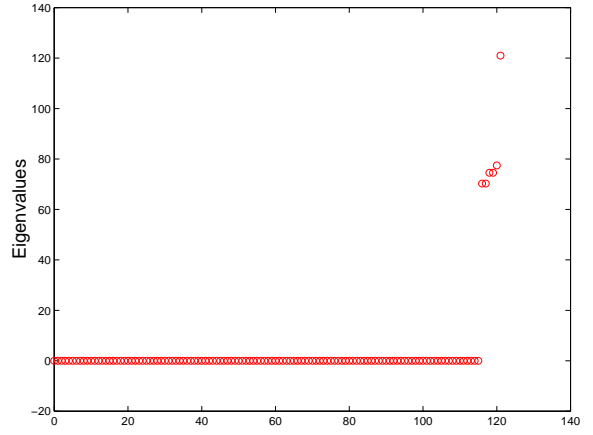


FIG. 4. The 122 eigenvalues for  $N = 11$ . There are six high values, corresponding to eigenvectors for which current is nonzero in the defect region.  $T_0 = 600nm$ ,  $R = 55nm$ .

## B. Calculating the vector potential

Having constructed the current basis, we can calculate the vector potential associated with each element of the current basis. In the discretized scheme, the vector potential is

$$\vec{A}(\vec{X}) = \frac{1}{c} \sum_{\vec{X}'}^{allspace} \frac{\vec{J}(\vec{X}')}{|\vec{X} - \vec{X}'|}. \quad (13)$$

In evaluating Eq.(13), one must include the contributions from all three types of current. Using the fact that  $\vec{J}(\vec{X} + \vec{\mathfrak{R}}) = \vec{J}(\vec{X})$ , where  $\vec{\mathfrak{R}}$  is a lattice translation vector, we can write

$$\vec{A}^j(\vec{X}) = \frac{1}{c} \sum_{j'=1}^3 \sum_{\vec{X}'}^{unitcell} \sum_{\vec{\mathfrak{R}}} \frac{\vec{J}^{j'}(\vec{X}')}{|\vec{X} - \vec{X}' + \vec{\omega}_j - \vec{\omega}_{j'} - \vec{\mathfrak{R}}|} \times \{1 - \delta_{\vec{\mathfrak{R}},0} \delta_{\vec{X},\vec{X}'} \delta_{j,j'}\}. \quad (14)$$

$\vec{\omega}_j$  is the displacement from the grid point  $\vec{X}$  to link  $j = 1, 2, 3$  inside the grid cell. To evaluate the slowly converging sum in Eq.(14), we use the Ewald trick<sup>18</sup>. Defining  $\xi \equiv |\vec{X} - \vec{X}' + \vec{\omega}_j - \vec{\omega}_{j'} - \vec{\mathfrak{R}}|$ , one uses the identity

$$\begin{aligned} \frac{1}{\xi} &= \frac{2}{\sqrt{\pi}} \int_0^\infty dt e^{-t^2 \xi^2} \\ &= \frac{2}{\sqrt{\pi}} \int_0^\eta dt e^{-t^2 \xi^2} + \frac{2}{\sqrt{\pi}} \int_\eta^\infty dt e^{-t^2 \xi^2} \\ &= \frac{1}{\xi} \text{erf}(\xi\eta) + \frac{1}{\xi} \text{erfc}(\xi\eta) \end{aligned} \quad (15)$$

to break up the sum into a long-ranged piece (the first integral) and a short-ranged part (the second integral).

The short-ranged term falls off rapidly for  $\xi \gg 1/\eta$ , and is readily computed. On the other hand, the long-ranged term converges slowly in real space. However, with the aid of two-dimensional form of Ewald's generalized theta function transformation<sup>18,19</sup>

$$\begin{aligned} & \int d^2 \vec{X} e^{-t|\vec{X} + \vec{\omega}_j - \vec{\omega}_{j'}|^2} e^{i(\vec{G} + \vec{K}) \cdot \vec{X}} \\ &= \frac{\pi}{t} e^{-i(\vec{G} + \vec{K}) \cdot (\vec{\omega}_j - \vec{\omega}_{j'})} e^{\frac{-|\vec{G} + \vec{K}|^2}{4t}}, \end{aligned} \quad (16)$$

the long-ranged term can be recast in a form that falls off rapidly with increasing  $\vec{K}$  in reciprocal space, making the sum tractable. (In this context,  $\vec{K} = N(u_1 \vec{W}_1 + u_2 \vec{W}_2)$ , where  $u_1$  and  $u_2$  are arbitrary integers.) The expression for  $\vec{A}^j(\vec{X})$ , formed by combining the short and long ranged pieces of the sum, converges reasonably quickly for an optimal choice of  $\eta$ . The total vector potential in the system due to supercurrents at link  $j$  of  $\vec{X}$  is the linear combination of  $\vec{A}_n^j(\vec{X})$ , i.e.,  $\vec{A}^j(\vec{X}) = \sum_n v_n \vec{A}_n^j(\vec{X})$ , where  $\vec{A}_n^j(\vec{X})$  is the vector potential associated with the  $n$ th element of the current basis  $\vec{J}_n^j(\vec{X})$  via Eq.(14).

### C. Minimizing the free energy in the presence of constraints

The Ginzburg-Landau theory yields a set of conditions that allow us to compute the currents and fields. We will see that these quantities minimize the London free energy while satisfying system constraints. In the limit that London theory is quantitatively valid, the current has the form as

$$\vec{J}(\vec{r}) = \frac{e^* n_s}{2m^*} \{ \hbar \vec{\nabla} \varphi(\vec{r}) - \frac{e^*}{c} \vec{A}(\vec{r}) \}, \quad (17)$$

where  $e^*$  is the superconducting electron charge,  $m^*$  the mass, and  $n_s$  the number of superconducting electrons per  $cm^3$ .  $\varphi(\vec{r})$  is the phase of the order parameter, and is therefore a single-valued function. Singularities in  $\varphi(\vec{r})$  at  $\vec{r}_i$  correspond to vortices:

$$\nabla^2 \varphi(\vec{r}) = \sum_i 2\pi \delta(\vec{r} - \vec{r}_i) p_i, \quad (18)$$

where  $p_i$  is the winding number for a vortex at  $\vec{r}_i$ . Using the expression for  $\vec{J}(\vec{r})$  given in Eq.(17), we find

$$\begin{aligned} \oint \vec{J}(\vec{r}) \cdot d\vec{l} &= \frac{e^* n_s}{2m^*} \{ \hbar \oint \vec{\nabla} \varphi(\vec{r}) \cdot d\vec{l} - \frac{e^*}{c} \oint \vec{A}(\vec{r}) \cdot d\vec{l} \} \\ &= \frac{\hbar c^2}{4\pi e^* \lambda^2} \{ \sum_i p_i - \frac{\Phi_B}{\phi_0} + P \}, \end{aligned} \quad (19)$$

where  $\phi_0 (= \hbar c / e^*)$  is superconducting magnetic flux quantum, and  $\Phi_B$  the magnetic flux contained in path.  $P$  is an integer which may arise in  $\oint \vec{\nabla} \varphi(\vec{r}) \cdot d\vec{l}$  for geometries

in which the superconductor is not simply connected. For example, integrating around a dot can give  $\oint \vec{\nabla} \varphi(\vec{r}) \cdot d\vec{l} \neq 0$  without any singularities. Minimizing the London free energy yields

$$\begin{aligned} & \vec{h}(\vec{r}) + \lambda^2 \vec{\nabla} \times \vec{\nabla} \times \vec{h}(\vec{r}) \\ &= \vec{h}(\vec{r}) + \frac{4\pi \lambda^2}{c} \vec{\nabla} \times \vec{J}(\vec{r}) = 0. \end{aligned} \quad (20)$$

Hence, for any path that does not enclose a net vortex charge, we have

$$\oint \vec{J}(\vec{r}) \cdot d\vec{l} = \frac{c}{4\pi \lambda^2} \oint \vec{A}(\vec{r}) \cdot d\vec{l}, \quad (21)$$

precisely as given by Eq.(19). Thus, it is sufficient to seek currents satisfying Eq.(19). By symmetry, the integral  $\oint_{cell} \vec{J}(\vec{r}) \cdot d\vec{l}$  vanishes if the integration contour is taken to be the unit cell boundary. From this condition, we see that

$$\frac{\Phi_{uc}}{\phi_0} = \sum_i p_i + P, \quad (22)$$

where  $\Phi_{uc}$  is the flux through the unit cell. Eq.(22) tells us that the magnetic field can only have the same periodicity as the dots if the number of flux quanta through a unit cell is an integer. For a thin-film superconductor, it is useful to write Eq.(19) in terms of the surface current density  $\vec{J}_s$  and  $\lambda_{eff}$ :

$$\oint \vec{J}_s(\vec{X}) \cdot d\vec{l} = \frac{\hbar c^2}{4\pi e^* \lambda_{eff}} \{ \sum_i p_i - \frac{\Phi_B}{\phi_0} + P \}. \quad (23)$$

Eq.(23) gives us two constraints to enforce:

$$\oint_{Dot} \vec{J}_s(\vec{X}) \cdot d\vec{l} = \frac{\hbar c^2}{4\pi e^* \lambda_{eff}} \{ P - \frac{\Phi_{Dot}}{\phi_0} \}. \quad (24)$$

and

$$\oint_{Sing} \vec{J}_s(\vec{X}) \cdot d\vec{l} = \frac{\hbar c^2}{4\pi e^* \lambda_{eff}} \{ \sum_i p_i - \frac{\Phi_{Sing}}{\phi_0} \}. \quad (25)$$

Within our network model,  $\oint \vec{J}_s(\vec{X}) \cdot d\vec{l}$  takes the form of a discrete sum which, when evaluated, depends only on the basis expansion coefficients  $v_n$ . The path of integration is the set of links making up the boundary of the defect, and  $\oint_{Dot} \vec{J}_s(\vec{X}) \cdot d\vec{l}$  is the sum of the inner product of the currents  $\vec{J}_s^j$  on the links and the links  $\vec{l}_0$ . In the case of Eq.(25), the integral about a singularity, the path consists of the six edges of the hexagon centered at  $\vec{X}$ , and  $\oint_{Sing} \vec{J}_s(\vec{X}) \cdot d\vec{l}$  is the sum of the six inner products  $\vec{J}_s^j \cdot \vec{l}_0$ . Fig. 5 depicts an example of the path of integration in the discrete scheme. In the figure, the path of integration about the defect contains 18 links, while paths about singularities are hexagonal, containing 6 links.

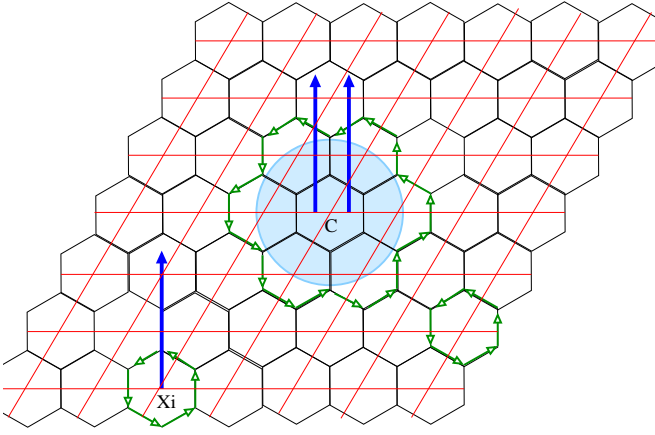


FIG. 5. The line integral paths around the dot located at  $\vec{C}$  and a singularity located at  $\vec{X}_i$ . Paths live on links. The border of the path around the dot consists of the 18 links making up the border of the defect. The path around the singularity is simply the border of the hexagonal plaquette centered at the singularity.

$\Phi_B$ , the magnetic flux enclosed by the path of integration, is

$$\begin{aligned}\Phi_B &= \int d^2 \vec{X} \cdot (\vec{h}_{ext}(\vec{X}) + \vec{h}_s(\vec{X})) \\ &= \int d^2 \vec{X} \cdot \vec{h}_{ext}(\vec{X}) + \oint d\vec{l} \cdot \vec{A}_s(\vec{X}).\end{aligned}\quad (26)$$

The vector potential  $\vec{A}_s(\vec{X})$  is calculated via Ewald method and is written in terms of  $\vec{J}_s(\vec{X})$ . In a manner similar to that described above for the current line integral, one can compute the line integral  $\oint d\vec{l} \cdot \vec{A}_s(\vec{X})$ . Again, the result depends only on the coefficients  $v_n$ . It is easy to calculate the flux due to the external magnetic field. One readily solves Eq.(22) for the applied field  $h_{ext}$ , finding

$$h_{ext} = \frac{\phi_0}{\alpha_{uc}} (\sum_i p_i + P), \quad (27)$$

where  $\alpha_{uc}$  is the area of the unit cell. Hence, we have for the external magnetic flux,

$$\int d^2 \vec{X} \cdot \vec{h}_{ext}(\vec{X}) = \frac{\alpha_{path}}{\alpha_{uc}} \phi_0 (\sum_i p_i + P), \quad (28)$$

where  $\alpha_{path}$  is the area enclosed by the line of integration. Inserting the right side of Eq.(28) into Eq.(24) and performing the discrete version of the line integral yields

$$\begin{aligned}l_0 \sum_n^{N^2+1-q} v_n \sum_{j=1}^3 \sum_{\vec{G} \neq 0} e^{-i\vec{G} \cdot \vec{C}} [\gamma^j(\vec{G}) J_n^j(\vec{G})] \\ = \frac{\hbar c^2}{4\pi e^* \lambda_{eff}} (P - N_0 \frac{\sum_i p_i + P}{N^2}).\end{aligned}\quad (29)$$

$\vec{C}$  locates the center of the defect.  $\gamma^j(\vec{G})$  is the sum of  $\vec{J}_s^j \cdot \vec{l}_0$ , and varies with the paths.  $N_0$  is the number of plaquettes enclosed by the path around the dot.

Similarly, the discrete version of Eq.(25) is

$$\begin{aligned}l_0 \sum_n^{N^2+1-q} v_n \sum_{j=1}^3 \sum_{\vec{G} \neq 0} e^{-i\vec{G} \cdot \vec{X}_i} [\eta^j(\vec{G}) J_n^j(\vec{G})] \\ = \frac{\hbar c^2}{4\pi e^* \lambda_{eff}} (p_i \delta_{\vec{X}, \vec{X}_i} - \frac{\sum_i p_i + P}{N^2}),\end{aligned}\quad (30)$$

where  $\eta^1 \equiv 1 - e^{i\vec{G} \cdot \vec{a}_1}$ ,  $\eta^2 \equiv 1 - e^{i\vec{G} \cdot \vec{a}_2}$ , and  $\eta^3 \equiv e^{i\vec{G} \cdot \vec{a}_2} - e^{i\vec{G} \cdot \vec{a}_1}$ .

Note that Eq.(30) holds for each of the plaquettes external to the dot, yielding a total of  $N^2 - (q+1)$  equations. Equations(29) and (30) allow us to solve uniquely for the coefficients  $v_n$ , permitting one to calculate the currents corresponding to a particular vortex configuration.

#### D. Solving for $v_n$ 's

Since the current in the system is given by  $\vec{J}_s^j(\vec{X}) = \sum_n v_n \vec{J}_n^j(\vec{X})$ , solving Equations(29) and (30) for the coefficients  $v_n$  is tantamount to finding the current distribution. As previously mentioned, we seek  $N^2 + 1 - q$  of the coefficients  $v_n$ , where  $q+1$  is the number of plaquettes comprising the defect. Eq.(29), and Eq.(30) represent a total of  $N^2 - q$  equations. However, it may be shown that only  $N^2 - (q+1)$  of these are independent.

Requiring that the net supercurrent vanish yields

$$\sum_n v_n j_{01}^n = 0 \quad (31)$$

and

$$\sum_n v_n j_{02}^n = 0. \quad (32)$$

One now has the desired  $N^2 + 1 - q$  independent linear equations for the coefficients  $v_n$ . In matrix form, we have

$$\begin{bmatrix} a_{11} & a_{12} & \cdots & a_{1i} & \cdots \\ a_{21} & a_{22} & \cdots & a_{2i} & \cdots \\ \vdots & \vdots & \ddots & \vdots & \ddots \\ a_{i1} & a_{i2} & \cdots & a_{ii} & \cdots \\ \vdots & \vdots & \ddots & \vdots & \ddots \end{bmatrix} \begin{bmatrix} v_1 \\ v_2 \\ \vdots \\ v_i \\ \vdots \end{bmatrix} = \begin{bmatrix} P - \frac{\sum_i p_i + P}{N^2} \\ 0 - \frac{\sum_i p_i + P}{N^2} \\ \vdots \\ p_i - \frac{\sum_i p_i + P}{N^2} \\ \vdots \end{bmatrix}. \quad (33)$$

The coefficients  $a_{ij}$  are found from Eqs.(29)-(32). Solving Eq.(33) yields the current distribution and, via Eq.(9), the free energy.

## IV. RESULTS

### A. Pinning Potentials

The freedom to control the locations of vortices in the unit cell permits the calculation of pinning potentials. The simplest case, in which a vortex interacts with a pinning center containing zero flux quanta, is displayed in Fig. 6. One can see that the vortex is strongly pinned by the dot because the potential drops discontinuously when the vortex enters the defect zone. The potential surface in the vicinity of the dot forms a potential well with a length scale set by the defect radius.

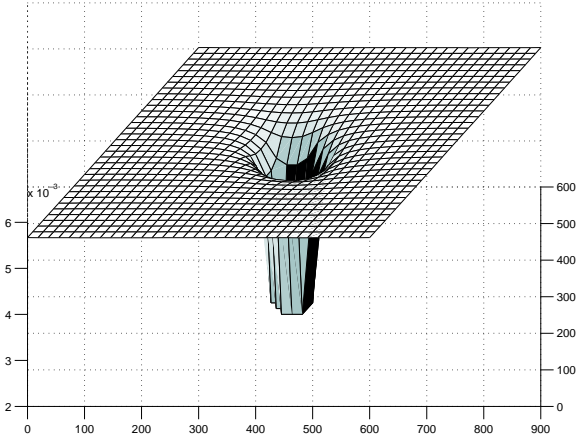


FIG. 6. Energy surface for a single vortex in the unit cell of antidots.  $T_0 = 600nm$ ,  $R = 0.06T_0$ ,  $\lambda = 1.5T_0$ .

Examining a cross section of the pinning potential allows one to infer the pinning energy, the energy required to dislodge a single vortex from the interior of the defect. Fig. 7 displays potential cross sections for defect radii spanning the range between the coherence length  $\xi(T)$  and  $\lambda_{eff}$ . A monotonic lowering of the pinning potential with increasing dot radius is evident from the plot. The graph in Fig. 7 supports the conclusion that the pinning energy initially increases rather swiftly as the radius of the defect increases beyond the coherence length.

Interesting physics arises when one computes the pinning potential for a vortex interacting with a defect containing a single flux quantum. The pinning potential for a typical case is shown in Fig. 8. The energy barrier surrounding the dot is perhaps the most salient qualitatively new feature compared to Fig. 7. The barrier tends to repel the external vortex from the defect zone. However if the vortex manages to cross the barrier, the pinning potential abruptly decreases and the vortex finds itself in a local minimum.

As the image indicates, another local minimum occurs at sites located at the centers of the equilateral triangles formed by the antidots. This interstitial minimum

is qualitatively very similar to that discussed in Ref. 16. As the darkened regions in Fig. 8 indicate, the interstitial pinning potential is quite shallow. Therefore, one expects a higher mobility for interstitially pinned vortices than for vortices captured by the dots.

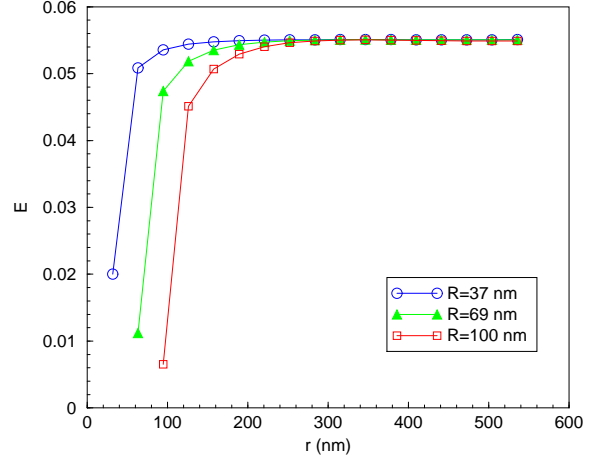


FIG. 7. Pinning Potentials for a single vortex in the unit cell of antidots with three different radii.  $T_0 = 600nm$ ,  $\lambda_{eff} = 90nm$ .

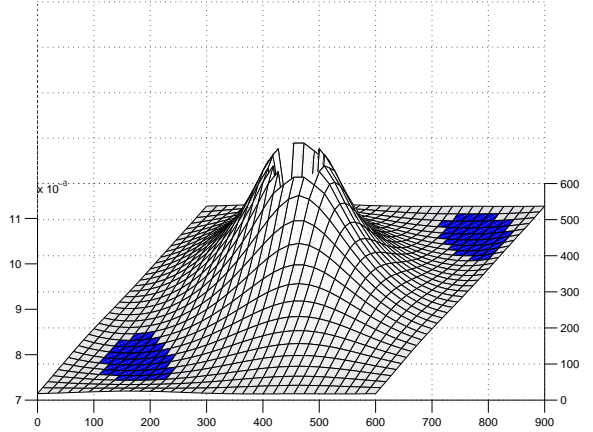


FIG. 8. Energy surface in the unit cell of saturated antidots ( $n_s = 1$ ).  $T_0 = 600nm$ ,  $R = 0.06T_0$ ,  $\lambda = 1.5T_0$ .

Fig. 9 displays a cross section of the single quantum pinning potential. The cross section is calculated along line A as illustrated in Fig. 1. The domain in the graph spans the distance between adjacent defects. Evidently, the presence of an energy barrier surrounding the dot necessitates the existence of an interstitial minimum. The inset offers a comparison with the case in which the pinning centers are not occupied by vortices. The pinning potential cross sections are qualitatively very similar to potentials calculated in Ref. 6 and Ref. 11.



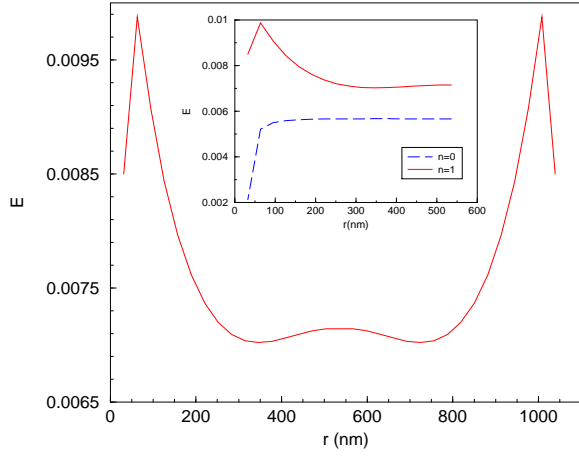


FIG. 9. Energy of vortex vs. the distance from the center of the antidot along line A in Fig. 1 when each dot is saturated with one vortex. The inset shows both curves for empty and saturated dots.

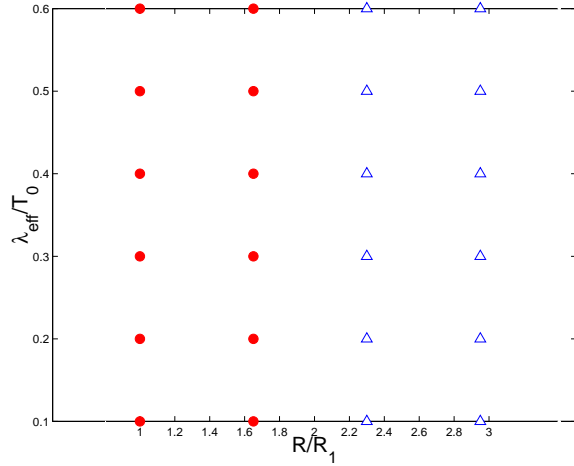


FIG. 10. Pinning phase diagram with weak dependence on  $\lambda_{eff}$ . The close-face squares represent the case of one captured vortex and one interstitial vortex, while the open-face triangles indicate that two vortices are captured.  $T_0 = 600nm$ ,  $R_1 = 0.05T_0$ .

Fig. 10 displays a pinning phase diagram. In the diagram the saturation number  $n_s$ , the number of flux quanta captured by the dot, is shown as a function of defect radius  $R$  and  $\lambda_{eff}$ . The phase diagram is plotted for fixed  $\xi(T)$ . Since the graininess of the discretization makes the notion of “radius” ambiguous, we take the defect radius to be the radius of the circle whose area is the same as the area enclosed by the defect boundary. A salient feature of the phase diagram is the absence of a strong dependence on the effective penetration depth,  $\lambda_{eff}$ <sup>20</sup>. In fact, the chief factor in the pinning phenomena

for fixed  $\xi(T)$  seems to be the defect radius. The dependence of  $n_s$  on  $R$  fits one’s intuition. For small values of  $R$ , it is energetically favorable for the dots to capture one vortex each, while the remaining vortex resides at the interstitial site. For larger defects, the two vortex capture scenario becomes increasingly favorable. When the dot is made larger than about 0.15 lattice constant, the trapping of two quanta prevails and  $n_s = 2$ .

## B. Pinning potentials for noncircular defects

It is interesting to examine pinning phenomena for cases in which the pinning center has an elongated structure. With the geometry of the triangular lattice, it is convenient to study defects in the shape of a rhombus, as illustrated in Fig. 11. It is informative to calculate pinning potentials in which a vortex interacts with defects containing a single flux quantum. The potential surface is depicted in Fig. 12. As for the circular case, energy minima appear near the centers of equilateral triangles formed by the defects. The structure of the interstitial sites, including the shallowness of the associated minima, is very similar to that of the circular case. As in the case of circular defects, the occupation of the rhombic defect by a vortex is associated with an energy barrier. However, the barrier in the rhombic case is distinguished by a marked anisotropy. The barrier near the acute-angled corners of the rhombus is lower than the barrier height at any other part of the defect boundary. One readily concludes that vortices tend to enter or leave defects through the sharper points. This phenomenon is reminiscent of the manner in which electrons on a conductor preferentially discharge from the region of greatest curvature.

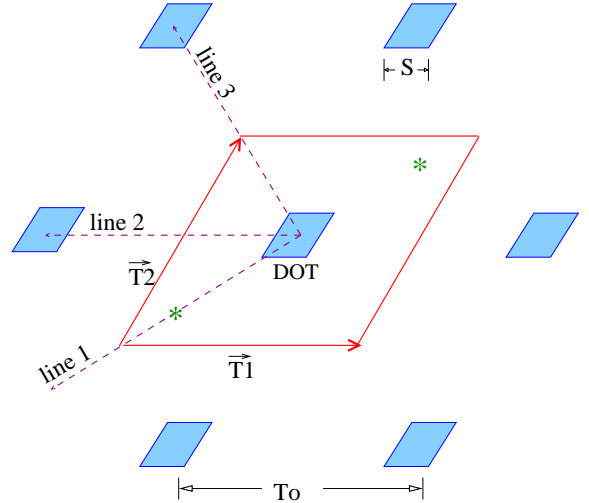


FIG. 11. The triangular lattice of antidots in the shape of rhombus. Each side of the dot has length  $S$ .



It is useful to compare the second capture energies of circular and rhombic defects of comparable area. (In this context, the  $N$ th capture energy is defined to be the shift in energy which occurs when a vortex is moved from the interstitial region to the interior of the defect to join  $N-1$  previously captured quanta.) To aid in the comparison, we display on the same plot pinning potential cross sections for defects with both circular and rhombic shapes in Fig. 13 and Fig. 14. The lone circular defect pinning potential is plotted along a radial line for the circular case. The 3 rhombic potentials shown on the same graph correspond to paths of approach which the reader can identify from Fig. 11. “Line 1” represents the easiest line of approach for the rhombus, in which one moves along the symmetry axis of the rhombus directly toward the sharpest corner of the defect. Two features of the potential are favorable for pinning. The “energy of approach”, defined as the energy needed to move the vortex to the crest of the energy barrier, is lower for the rhombic defect than for the circular dot. The potential also indicates a greater pinning energy for rhombic defects. In fact, Fig. 14 displays a case in which it is favorable for a rhombic defect to capture two flux quanta while its circular counterpart is only able to capture a single vortex. The lower energy of approach ensures faster kinetics, hence swifter vortex capture for elongated pinning centers. The greater pinning energy, on the other hand, ensures that the vortices remain trapped once captured.

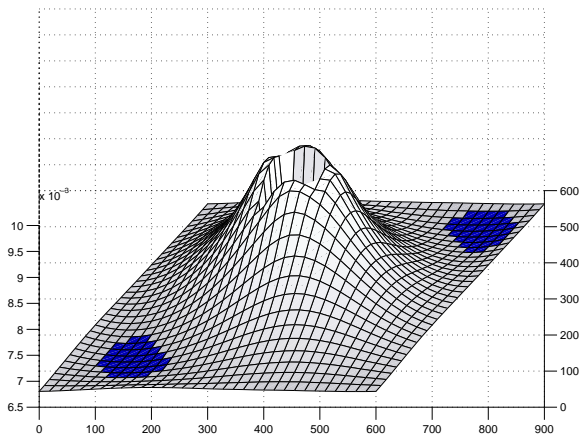


FIG. 12. Energy surface for a single vortex in the unit cell of saturated rhombic defects containing one vortex each ( $n_s = 1$ ).  $T_0 = 600nm$ ,  $S \sim 0.16T_0$ ,  $\lambda = 1.5T_0$ .

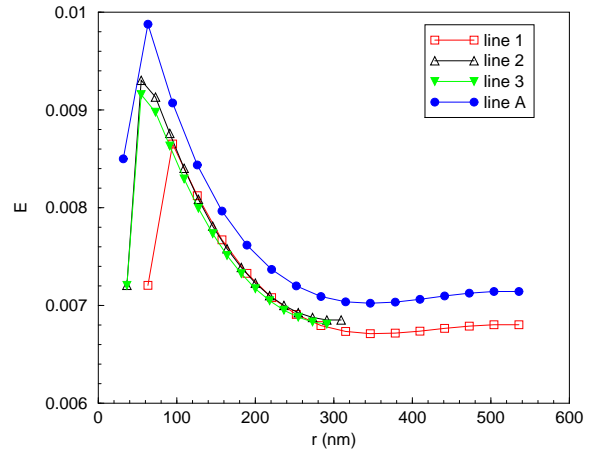


FIG. 13. Energy of vortex vs. the distance from the center of the antidot along line A in Fig. 1, line 1, line 2 and line 3 in Fig. 11 when each dot is saturated with one vortex.  $T_0 = 600nm$ ,  $\lambda_{eff} = 1.5T_0$ ,  $S = 2R \sim 0.16T_0$ .

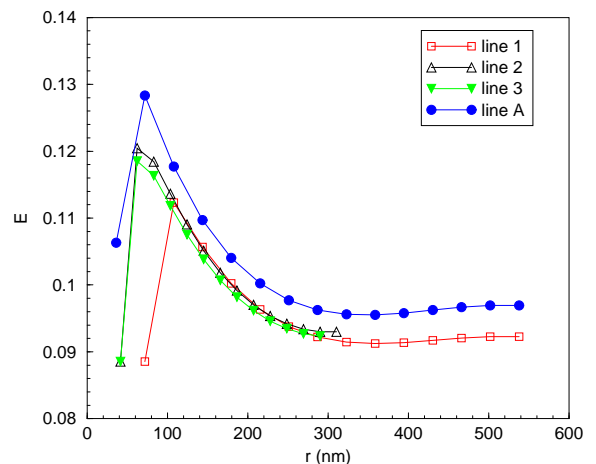


FIG. 14. Energy of vortex vs. the distance from the center of the antidot along line A in Fig. 1, line 1, line 2 and line 3 in Fig. 11 when each dot is saturated with one vortex.  $T_0 = 600nm$ ,  $\lambda_{eff} = 0.1T_0$ ,  $S = 2R \sim 0.16T_0$ .

## V. SUMMARY

In the work described in this report, we have used a wire network model to provide a detailed treatment of pinning phenomena in nanoscale defect arrays. Our results are consistent with experiments involving thin-film superconductors and are qualitatively very similar to theoretical work on three dimensional superconductors containing columnar defects.

A comparison of pinning potentials suggests that elongated pinning centers have superior pinning characteristics to similar sized circular defects.

Future work will extend this study to more general defect types and lattice geometries. We have fashioned techniques that permit the study of films with nontrivial three dimensional structures. Many of the experiments performed on nanoscale defect arrays are neither deep in the thin-film limit nor in the bulk limit. To model these systems properly, it is necessary to go beyond the thin-film approximation and provide a detailed three dimensional treatment of the superconducting films. Such studies will be presented in future work.

## ACKNOWLEDGMENTS

The authors would like to thank Professor Lance DeLong for useful discussions concerning this research. This work was supported by NSF Grant No. DMR-9870681 and DMR-0108451.

- <sup>11</sup> I. B. Khalfin and B. Ya. Shapiro, *Physica C* **207**, 359 (1993).
- <sup>12</sup> A. I. Buzdin, *Phys. Rev B* **47**, 11416 (1993).
- <sup>13</sup> C. Reichhardt, J. Groth, C. J. Olson, S. B. Field, and F. Nori, *Phys. Rev. B*, **54**, 16108 (1996).
- <sup>14</sup> C. J. Olson, C. Reichhardt, and F. Nori, *Phys. Rev. Lett.* **81**, 3757 (1998).
- <sup>15</sup> N. Takezawa and K. Fukushima, *Physica C* **228**, 149 (1994).
- <sup>16</sup> C. Reichhardt, C. J. Olson, and F. Nori, *Phys. Rev. B* **57**, 7937 (1998).
- <sup>17</sup> P. G. de Gennes, *Superconductivity of metals and alloys* (Addison-Wesley, New York, 1966).
- <sup>18</sup> P. P. Ewald, *Ann. Phys. (Leipz.)* **54**, 519 (1917); **54**, 557 (1917); **64**, 253 (1921).
- <sup>19</sup> Lynn Bonsall, A. A. Maradudin, *Phys. Rev. B* **15**, 1959 (1977).
- <sup>20</sup> It can be shown that some dependence of  $n_s$  on  $\lambda_{eff}$  does exist. These calculations will be presented elsewhere.

- 
- <sup>1</sup> V. V. Metlushko, M. Baert, R. Jonckheere, V. V. Moshchalkov, and Y. Bruynseraede, *Solid State Commun.* **91**, 331 (1994).
  - <sup>2</sup> V. V. Moshchalkov, L. Gielen, M. Baert, V. Metlushko, G. Neuttiens, C. Strunk, V. Bruyndoncx, X. Qiu, M. Dhallé, K. Temst, C. D. Potter, R. Jonckheere, L. Stockman, M. Van Bael, C. Van Haesendonck, and Y. Bruynseraede, *Phys. Scr.* **I55**, 168 (1994).
  - <sup>3</sup> M. Baert, V. V. Metlushko, R. Jonckheere, V. V. Moshchalkov, and Y. Bruynseraede, *Europhys. Lett.* **29(2)**, 157 (1995).
  - <sup>4</sup> M. Baert, V. V. Metlushko, R. Jonckheere, V. V. Moshchalkov, and Y. Bruynseraede, *Phys. Rev. Lett.* **74**, 3269 (1995).
  - <sup>5</sup> K. Harada, O. Kamimura, H. Kasai, T. Matsuda, A. Tonomura, and V. V. Moshchalkov, *Science* **274**, 1167 (1996).
  - <sup>6</sup> V. V. Moshchalkov, M. Baert, V. V. Metlushko, E. Rosseel, M. J. Van Bael, K. Temst, R. Jonckheere, and Y. Bruynseraede, *Phys. Rev. B* **54**, 7385 (1996).
  - <sup>7</sup> V. V. Moshchalkov, M. Baert, V. V. Metlushko, E. Rosseel, M. J. Van Bael, K. Temst, Y. Bruynseraede, and R. Jonckheere, *Phys. Rev. B* **57**, 3615 (1998).
  - <sup>8</sup> V. V. Metlushko, L. E. DeLong, M. Baert, E. Rosseel, M. J. Van Bael, K. Temst, V. V. Moshchalkov, and Y. Bruynseraede, *Europhys. Lett.* **41(3)**, 333 (1998).
  - <sup>9</sup> See <http://www.bell-labs.com/new/gallery/shpm.html>.
  - <sup>10</sup> S. B. Field, S. S. James, J. Barentine, V. Metlushko, G. Crabtree, H. Shtrikman, B. Ilic, and S. R. J. Brueck, *arXiv:cond-mat/0003415* v1 25 Mar 2000.